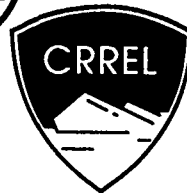


91-11

CRREL REPORT

DTIC
SELECTE
AUG 07 1991
S D D

2



This document has been approved
for public release and sale; its
distribution is unlimited.

Interpretation of Passive Microwave Imagery of Surface Snow and Ice Harding Lake, Alaska

Rae A. Melloh, Duane T. Eppler, L. Dennis Farmer,
Lawrence W. Gatto and Edward F. Chacho

June 1991

AD-A239 140



91-06998



91 8 05 162

For conversion of SI metric units to U.S./British customary units of measurement consult ASTM Standard E380, Metric Practice Guide, published by the American Society for Testing and Materials, 1916 Race St., Philadelphia, Pa. 19103.

Cover: KRMS Image of Harding Lake.



**U.S. Army Corps
of Engineers**
Cold Regions Research &
Engineering Laboratory

Interpretation of Passive Microwave Imagery of Surface Snow and Ice Harding Lake, Alaska

Rae A. Melloh, Duane T. Eppler, L. Dennis Farmer,
Lawrence W. Gatto and Edward F. Chacho

June 1991



Accession For	
NTIS CRA&I	<input checked="" type="checkbox"/>
DTIC TAB	<input type="checkbox"/>
Unannounced	<input type="checkbox"/>
Justification	
By	
Distribution	
Availability Codes	
Dist	Availability or Special
A1	

PREFACE

This report was prepared by Rae A. Melloh, Research Physical Scientist, Lawrence W. Gatto, Geologist, and Edward F. Chacho, Research Civil Engineer, of the Geological Sciences Branch, Research Division, U.S. Army Cold Regions Research and Engineering Laboratory; and Dr. Duane T. Eppler and L. Dennis Farmer of the Naval Oceanographic and Atmospheric Research Laboratory. Funding for this investigation was provided by CRREL's In-House Laboratory Independent Research Program under ILIR effort 499/500, *Interpretation of River and Lake Ice from Airborne KRMS and SAR Imagery*.

The authors thank Charles Collins and Anthony Zenk of CRREL-Alaska for their assistance in collection of ground truth data; Dr. Matthew Sturm of CRREL-Alaska for assistance with snow pit data; Dr. Steven Arcone and Allan Delaney for acquiring the impulse radar trace; and Bruce Heydlauff of the Naval Weapons Center, China Lake, California, whose expertise with the KRMS instruments and data reduction equipment was essential to the success of the mission. They also thank Dr. Alan Lohanick and Walter Tucker for their technical review of this manuscript and Dr. Anthony Gow for his review of Appendix B.

CONTENTS

	Page
Preface	ii
Introduction	1
Geographic setting	1
K _a -band radiometric mapping system	2
Image analysis	2
Surface conditions	2
Relationships between surface conditions and image patterns	9
Radiometric explanations for image tones and patterns	11
Conclusions	14
Literature cited	14
Appendix A: KRMS description	17
Appendix B: Ice cores	21
Abstract	31

ILLUSTRATIONS

Figure

1. Location of Harding Lake	2
2. KRMS pod hanging from the bomb bay of an RP-3 aircraft	2
3. Conditions during aerial flights and ground-truth data collection	3
4. Photomosaic from aerial video tape of 17 March	4
5. Ice core and impulse radar transect across Harding Lake	5
6. Profile of ice thickness and depth to bed	5
7. Linear snow ice feature observed during placement of aluminized Mylar targets on 10 March	5
8. Impulse radar acquired by Dr. S. Arcone and A. Delaney of CRREL	6
9. Daily maximum and minimum air temperatures at Eielson Air Force Base and Big Delta	7
10. Hourly air temperatures at Eielson Air Force Base and Big Delta prior to and during the KRMS flights	7
11. Distribution of snow on the lake surface	8
12. Equivalently scaled KRMS images	10
13. KRMS images of Birch and Quartz lakes	11
14. Variation of snow penetration depth with liquid water content	11
15. Calculated brightness temperature of snow-covered terrain for volumetric water contents of 0% and 2%, for a snow cover of 50 cm	12
16. Color density slice of 8 and 11 March images show the change in approximate brightness temperature	12
17. Brightness temperature of a wind drift type snow of 62-cm depth and 14-cm water equivalent	13
18. Brightness temperature of a depth hoar type snow of 59-cm depth and 14.2-cm water equivalent	13

TABLES

Table

1. KRMS technical characteristics	3
2. KRMS radiometric temperatures near nadir	11
3. Scaled KRMS temperatures and color assignments	12

Interpretation of Passive Microwave Imagery of Surface Snow and Ice Harding Lake, Alaska

RAE A. MELLOH, DUANE T. EPPLER, L. DENNIS FARMER,
LAWRENCE W. GATTO AND EDWARD F. CHACHO

INTRODUCTION

Passive microwave imagery can provide information about freshwater ice and snow environments necessary for studies of geophysical processes in rivers and lakes. Microwave sensitivity to surface roughness and ability to penetrate through the volume of snow and ice allow observations that could not be made with shorter wavelength visible and infrared systems. The ability to image both through cloud covers and at night is an additional advantage of microwave over shorter wavelength systems. Although previous studies have provided some answers regarding the relationship between field conditions and passive microwave image patterns (Schmugge et al. 1973 and Hall et al. 1978, 1981), the range of conditions that have been studied is limited and the level of detail of interpretations has often been restricted by limited ground truth or conditions too complex to adequately describe. Consequently, the combination of snow and freshwater ice conditions that produce image patterns is only partially understood and the value of passive microwave data in geophysical studies is not fully known.

The ability to distinguish freshwater ice and snow conditions in microwave imagery depends on the characteristics of the sensor system and the physical properties of the materials. Passive systems measure naturally emitted radiation in terms of brightness temperature (T_B), which is the product of the physical temperature (T_o) of an object and its emissivity (E) at the wavelength being sensed ($T_B = ET_o$). The ability to distinguish freshwater ice conditions in an environment with little physical temperature variation depends largely on differences in emissivity. For example, smooth, open water surfaces have a very low emissivity, resulting in the lowest brightness temperatures in a scene, while wet

snow is highly emissive, resulting in a much warmer signature. Investigations using passive systems over freshwater lake ice have shown that shorter wavelength (0.81-cm) radiometers are better suited for gathering information about the upper layers of ice and snow on the surface, while longer wavelengths (6 cm) may sense conditions involving the entire ice thickness (Hall et al. 1981).

In this study we correlate known surface snow and ice conditions on Harding Lake near Fairbanks, Alaska, with gray tones and patterns on images acquired by the K_a -band Radiometric Mapping System (KRMS). The KRMS imagery obtained on 8 and 11 March 1988 allows a comparison of brightness temperature patterns of dry and wet snow conditions. This study is part of an ongoing investigation to evaluate both active and passive microwave systems, of various wavelengths and polarizations, for their ability to distinguish river and lake ice conditions (Melloh and Gatto 1990a, b).

GEOGRAPHIC SETTING

Harding Lake is located about 60 km southeast of Fairbanks and about 160 km south of the Arctic Circle (Fig. 1). The lake is roughly circular in shape and has a surface area of about 10 km² at an elevation of 218 m above mean sea level. The maximum depth of the lake is around 43 m and the average depth is 16 m. Harding Lake is positioned at the boundary between the Yukon-Tanana Upland and the Middle Tanana River Valley; the lake is underlain by the Tanana gravel formation on the north and the Birch Creek schist formation on the south (Nakao 1980). The climate is continental, typified by extremely cold winters and cool summers; the mean January air temperature is around -25°C and the mean annual air temperature is around -4°C.

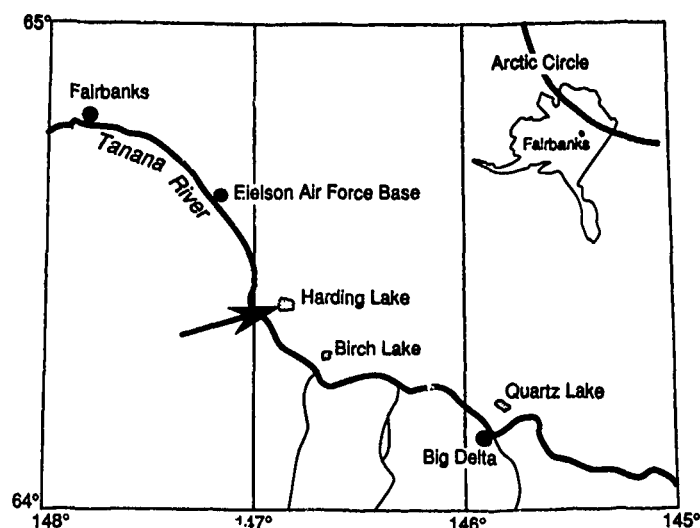


Figure 1. Location of Harding Lake.



Figure 2. KRMS pod hanging from the bomb bay of an RP-3 aircraft. (Photograph by D. Farmer, December 1981.)

K_a-BAND RADIOMETRIC MAPPING SYSTEM

The KRMS is an airborne passive microwave imager that operates at a center frequency of 33.6 GHz (Table 1) or a wavelength of 0.89 cm. The instrument is pod mounted and hangs from the bomb bay of an RP-3 aircraft (Fig. 2). The KRMS system has been extensively used in polar ice research in differentiating surface types such as open water, first-year ice and multiyear ice

(Eppler et al. 1984). This report discusses the first application of the KRMS for analyzing freshwater ice conditions. Appendix A provides details of how the KRMS system acquires microwave radiance data and how the data are processed to brightness temperatures.

IMAGE ANALYSIS

Analysis of the data collected at Harding Lake is presented in three steps: 1) surface conditions on the lake during the flights are described, 2) the known surface conditions are related to microwave image tones and patterns, and 3) the tones and patterns are explained in terms of microwave emission and scattering within the snow and ice layers.

Surface conditions

Ground observations and measurements of the physical properties and stratigraphy of the snow and ice materials were collected at specific sites on 3 and 10 March while aerial photographs (1 March) and videotapes (17 March) were taken to document the spatial distribution of snow on the lake surface (Fig. 3). Ice thickness and volume characteristics were determined from ice cores taken on 3 March (App. B). An impulse radar trace was acquired on 16 March to distinguish floating from grounded ice. Distribution of snow on the

Table 1. KRMS technical characteristics (Eppler et al. 1984).

Antennas	
number	3
diameter	0.61 m
polarization	Vertical
beam width	1.0°
isolation	40 dB (minimum)
Scanner	
maximum scan rate	25 scans/second (40 ms/scan)
minimum scan rate	7.5 scans/second (133 ms/scan)
scan angle	60° from nadir
midscan incidence angle	0° (nadir)
scan width	3.46 × altitude
antenna position accuracy	2.5 minutes of arc
Stabilization	
method	Cross-track roll gyro
accuracy	Less than 0.25°
RF amplifier	
type	Superheterodyne (DSB)
noise	Less than 5.0 dB
bandwidth	1.3 GHz
gain	Greater than 60 dB
loss	1.2 dB (maximum)
Radiometer	
type	Pulse stabilized, total power
pulse width	4.0 ms
local oscillator frequency	33.6 GHz
IF bandwidth	Greater than 500 MHz
video bandwidth	1.7 kHz (maximum)
video gain	72 dB (nominal)
minimum detectable signal	0.05 K/second
sensitivity	50 mV/K (nominal)
dynamic range	370 K

lake surface is documented on a photomosaic (Fig. 4) made from individual frames of an aerial videotape acquired on 17 March at an elevation of 1500 m.

Ice

On 3 March, ice conditions were observed and measured along a transect crossing the lake from the northwest to southeast (Fig. 5). To an observer standing on the surface, areas without snow cover appeared as either spectacularly clear ice with vertical fractures extending through the entire ice thickness, or a bubbly surface ice that produced varying degrees of opacity. Correspondingly, ice cores consisted predominantly of clear massive lake ice without extensive bubbles or visible impurities, but were often capped by a layer of granular snow ice (App. B). The thickness of the floating ice varied from 69 to 84 cm, averaging 76 cm (Fig. 6). The transect was chosen to pass over a shallow shelf where different patterns or tones might result on the KRMS imagery. Comparisons of thin sections of the ice cores show a 3- to 5-cm thicker granular ice layer in the core taken over the shelf (App. B). Snow ice is a granular white ice formed from refreezing of melted snow or from later incursions of lake water into the snow cover through cracks in the ice sheet. The incursion process is described on a subarctic lake by Shaw (1965).

Ice surface observations were made again on 10 March during placement of 6- × 12-m aluminized Mylar targets. The targets were placed with the intent of pinpointing features observed on the 8 March KRMS im-

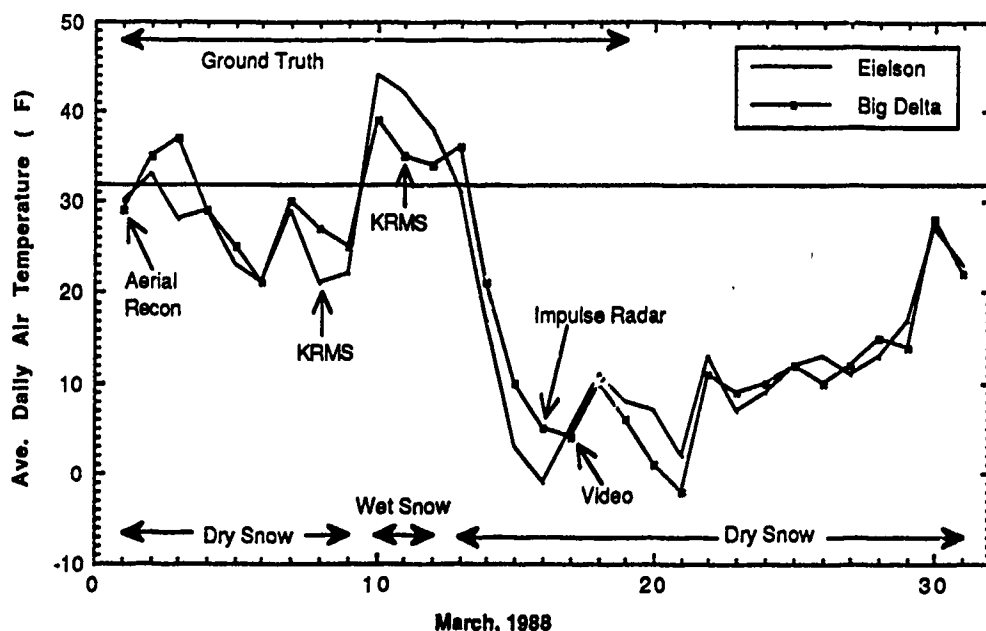
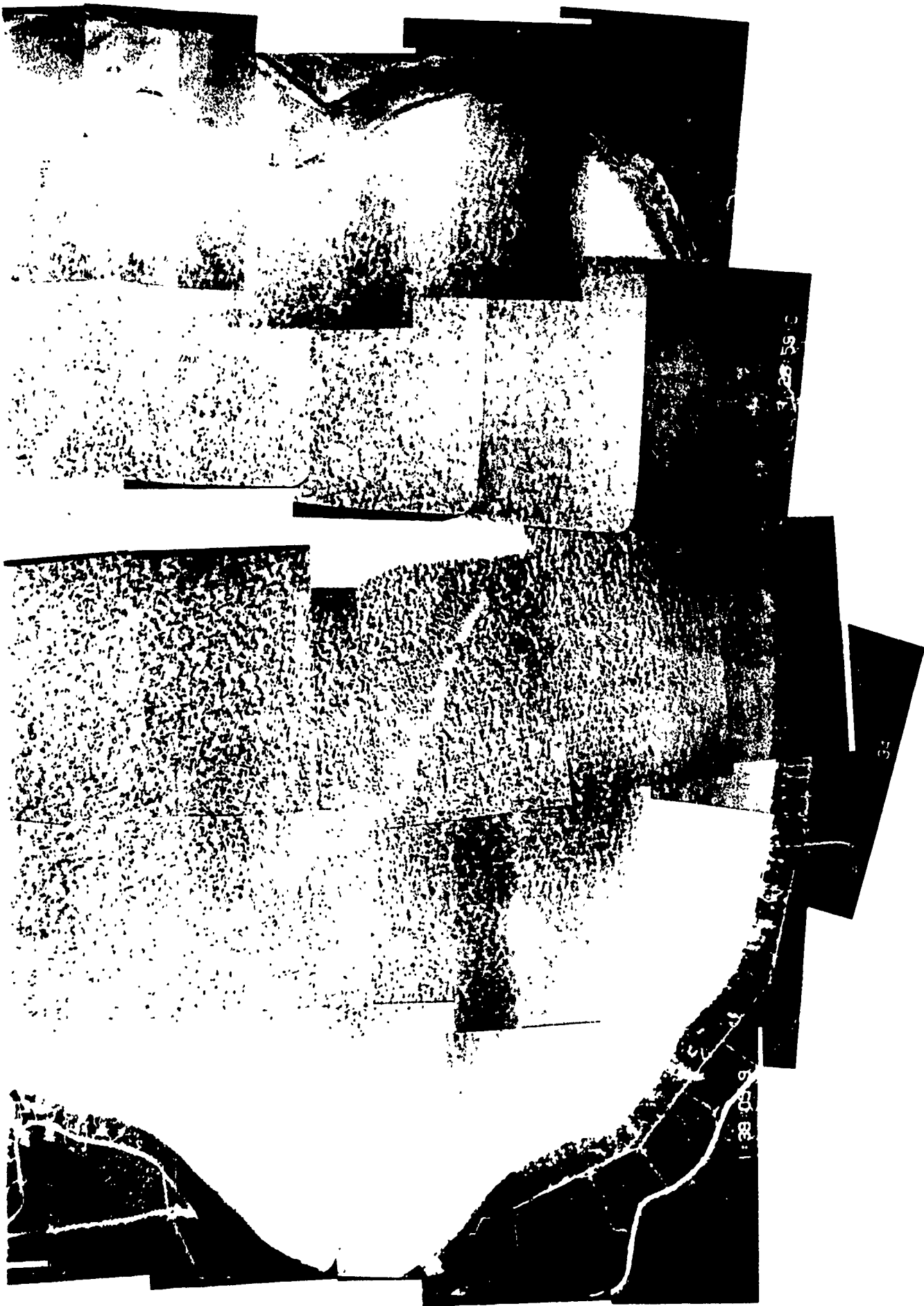


Figure 3. Conditions during aerial flights and ground-truth data collection.



10/9
Figure 4. Photomosaic from aerial v



4 Photomosaic from aerial video tape of 17 March

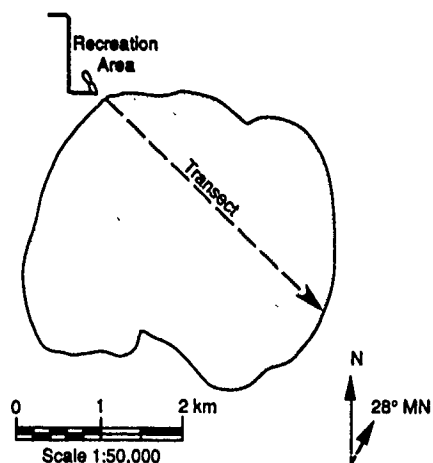


Figure 5. Ice core and impulse radar transect across Harding Lake, at a heading of 134°.

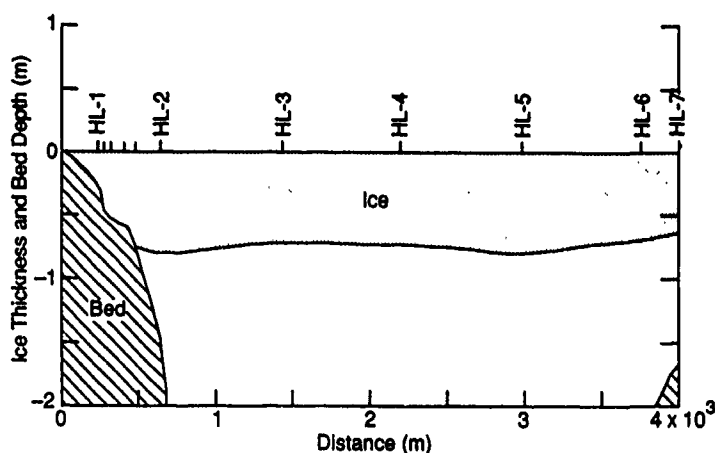


Figure 6. Profile of ice thickness and depth to bed. Location of ice core and other thickness measurement sites are indicated.



Figure 7. Linear snow ice feature observed during placement of aluminized Mylar targets on 10 March. The arrow in the center of the photograph points along the snow ice feature.

age. The first surface type targeted was a linear snow ice feature estimated to be 65 m wide and having the appearance of melted snow refrozen on the ice surface (Fig. 7). The linear patterns on the 8 March KRMS image suggested that these snow ice features formed above cracks in the ice sheet through which water rose by capillary action into the overlying and nearby snowpack.

A similar, localized formation of 2- to 3-in.-high mounds of snow ice on a subarctic lake in Quebec is described by Shaw (1965). The second target was placed on a particularly large black ice surface. The snow cover had been redistributed by the wind; the black-ice surfaces occurred in pockets of essentially snow-free ice. The targeted features could not be discerned on the 11 March

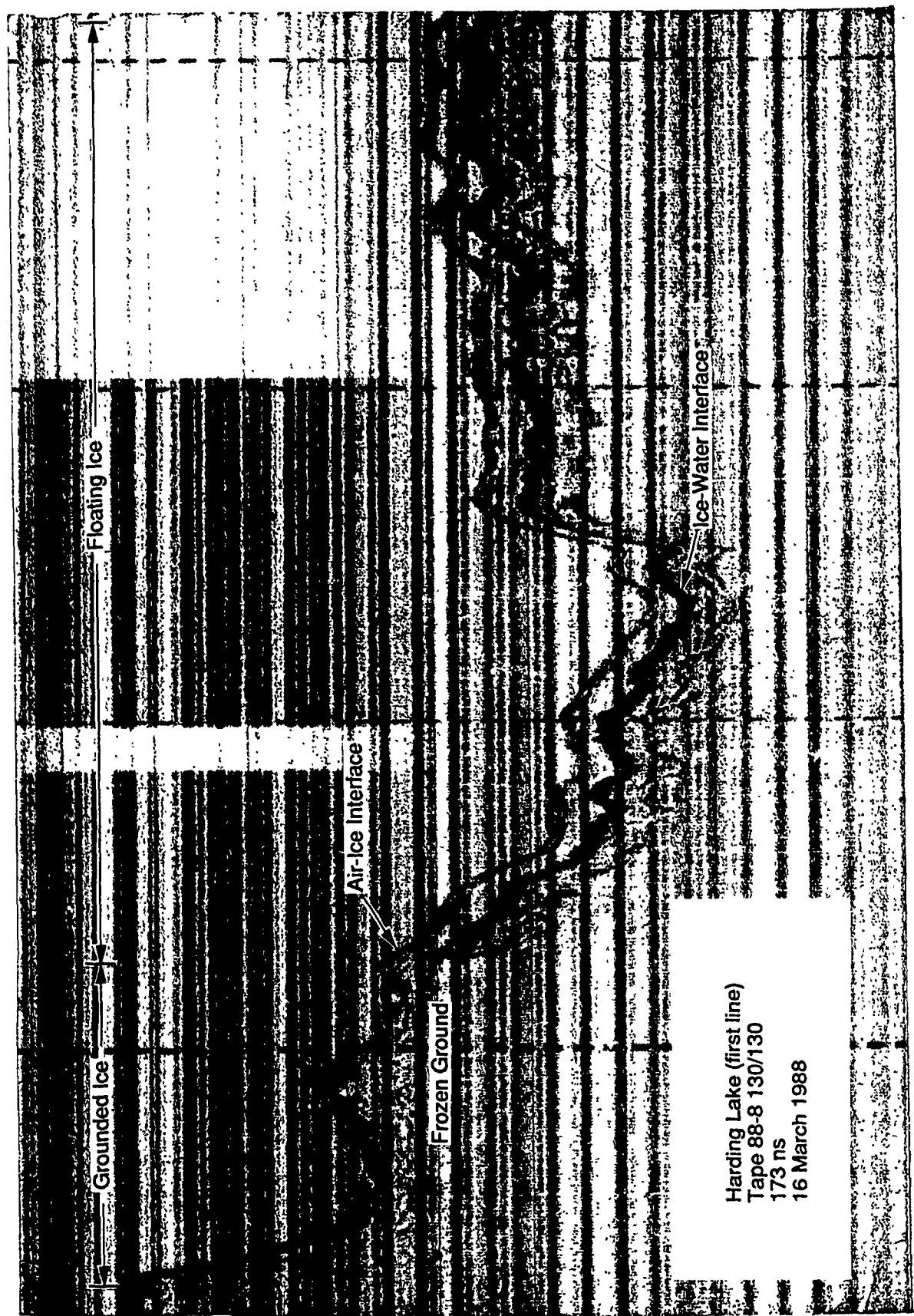


Figure 8 Impulse radar trace acquired by Dr. S. Arcone and A. Delaney of CRREL. The unlevel surface of the trace is due to variations in the height of the helicopter.

image because of unexpected wet snow conditions and the resulting lack of radiometric contrast of the features with the adjacent lake surface.

Interpretation of a radar trace acquired by Arcone and Delaney (1987) on 18 March with a 500-MHz short pulse radar mounted on a helicopter and flown along the transect reveals that the ice sheet was frozen to the shelf for a considerable distance lakeward from the shoreline (Fig. 8). High contrast in dielectric permittivities of ice (3.2) and water (87) at 500 MHz results in a strong reflection of the pulsed radar; hence, dark returns appear on the printed trace. Where the ice was frozen to the bed, little return appears on the trace. Frozen sand and gravel bed materials have dielectric permittivities nearer that of ice; hence, reflection from the ice-bed interface was relatively small. Distances cannot be accurately measured on the trace, but the lakeward margin of the grounded ice was estimated at 400 to 500 m offshore by drilling through the ice on 3 March (Fig. 6).

Snow

Snow depths were measured around each ice core site on 3 March. The snow had drifted into dunes over much

of the transect. Dune heights were estimated (10 March) to range from 10 to 30 cm in maximum height, with the average dune around 20 cm. The stratigraphy of one of the dunes consisted of a surface layer of windblown snow consisting of sub-millimeter rounded grains overlying depth hoar crystals that ranged from 1 to 2 mm at the top of the pack to 8 mm lower in the pack. A thin basal layer contained depth hoar crystals as long as 20 mm. Measured snow density in the wind-blown layer was 0.41 g/cm^3 and near the base of the snow, 0.20 g/cm^3 . Active melting of the snowpack was observed on 10 March, as evidenced by thin puddles or veneers of melting snow on adjacent snow-free ice and ablation hollows or "suncups" (Gray and Male 1981) formed on the snow surfaces. The surface of the snow was wet or damp, exhibiting large necks between the grains.

The spatial variation of the snow cover was also observed (1 and 3 March). The snow dunes were higher in the middle and northern end of the transect. Snowdrifting caused the snow cover to be continuous and deeper near the northwest shore. The snowpack was old; the most recent snowfall prior to the KRMS overflights had been about 2.5 cm on 20 February (NOAA 1989) with only light snows occurring earlier in January and February. Depths of snow on the ground were reported as only 5 cm at Big Delta and 25.4 cm at Eielson during the first week of March.

Weather station data at Big Delta and Eielson indicated changing snow conditions during the field experiment. Air temperatures between 1 and 9 March attained maximums above and minimums below freezing (Fig. 9). Hourly air temperatures preceding and during the 8 March KRMS flight (Fig. 10) were below freezing at Eielson, but slightly above freezing at Big Delta, suggesting that the snow on Harding Lake was dry during

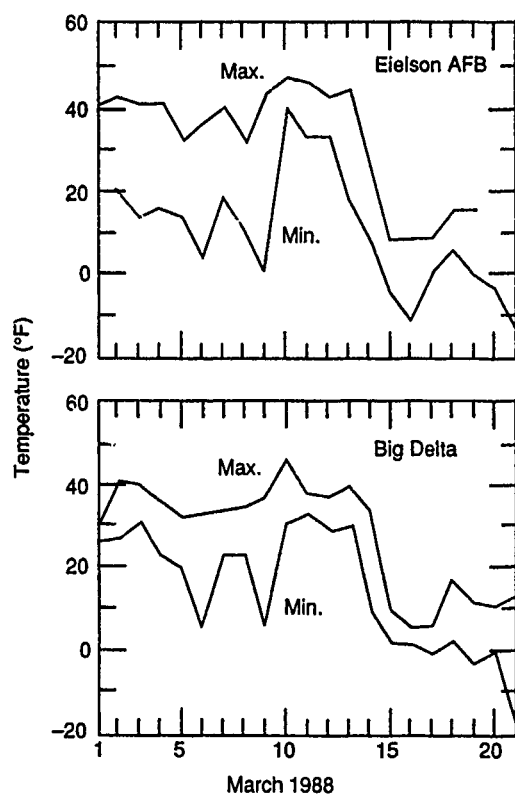


Figure 9. Daily maximum and minimum air temperatures at Eielson Air Force Base (top) and Big Delta (bottom).

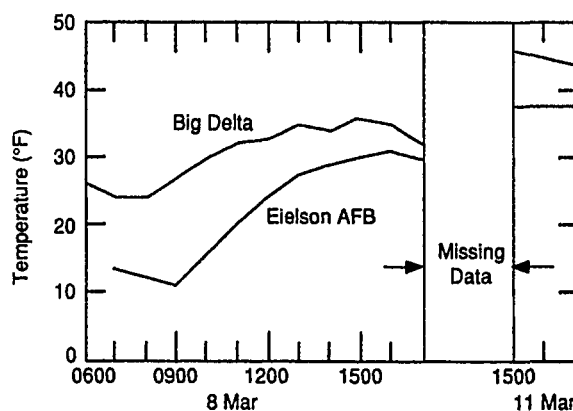
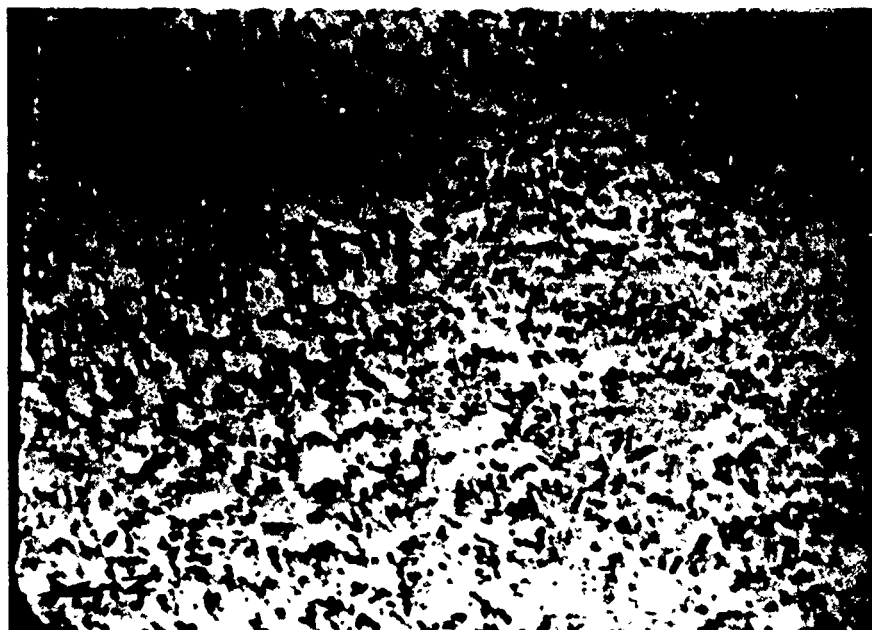


Figure 10. Hourly air temperatures at Eielson Air Force Base and Big Delta prior to and during the KRMS flights (provisional data provided by NWS Forecast Office, Fairbanks, Alaska).

the first flight. Above-freezing minimum daily temperatures on 10 March (Fig. 9) and hourly temperatures preceding the second flight (Fig. 10) suggest that the snow was wet when imaged on 11 March. Following the KRMS flight on 11 March and prior to the aerial video flight on 17 March, air temperatures dropped sharply

between 12 and 15 March and remained low through 17 March (Fig. 9). Light snowfalls were recorded at Eielson on 15 March (3 cm) and at Big Delta on 16 March (3.8 cm), but not in sufficient amounts to change the areal distribution as observed during the previous week.



a. 17 March aerial video frame.



b. 1 March airphoto.

Figure 11. Distribution of snow on the lake surface.

Aerial videotapes taken on 17 March show the distribution of snow cover on the lake six days after the last KRMS flight. The texture of the snow cover of the 8 and 11 March flight dates is discernible on the video mosaic (Fig. 4) and is similar to the snow distribution observed during the aerial reconnaissance on 1 March (Fig. 11). The snow had been blown into snow dunes similar to crescent-shaped barchan dunes. The snow dunes were oriented with their longitudinal dimensions predominantly north-south, at an oblique angle of roughly 45° with the KRMS flight path. The texture of the snow cover is coarsest in the lake center where large, well-defined snow-dunes and adjacent pockets of snow free ice occur. Larger dunes measure roughly 30 × 40 m on the mosaic. The snow cover grades into a finer texture toward the shoreline where smaller snow dunes occur and snow cover is more complete (Fig. 4).

Relationships between surface conditions and image patterns

The 8 March KRMS image of Harding Lake (Fig. 12a) can be divided into three major surface types. Type 1, making up the majority of the lake surface, is a radiometrically cool (medium- to light-toned) background. Type 2 is made up of numerous radiometrically warm (dark-toned) linear features contrasting with the background. Type 3 is a separate, cold (light-toned) band that is widest around the northwest nearshore zone of the lake, but extends all along the shoreline. The three types are discernible on the 11 March image (Fig. 12b), but less so. Notable differences are that fewer linear features are discernible on the 11 March image, the linear features are radiometrically warmer (darker) than the background on 8 March but are slightly cooler (lighter) than the background on 11 March, and the radiometrically cold (light-toned) band is far less distinct on the 11 March image. Relating the image tones and patterns to known field conditions leads to the following interpretations.

Type 1

The background surface corresponds to fields of snow dunes and adjacent snow-free ice that produce the mottled texture on the aerial video mosaic but a uniform, gradually varying tone on the KRMS images. The KRMS footprint, approximately 26.6 m in diameter at nadir and 1500-m flight altitude, is large enough relative to the dunes and snow-free ice that the radiances of the two surfaces often combine. Pixel by pixel radiances are further homogenized by integration along the scan line due to the sampling interval and across the scan line due to the nominal 80% cross-scan overlap of the beamspot (see App. A).

Gradual tonal changes of the background occur both vertically and horizontally across the image. The gradual tonal change of the background from radiometrically colder (lighter), along a vertical center-line of the image, to radiometrically warmer (darker), toward the left and right edges, is most apparent on the 11 March image, and is largely due to the incidence angle effect along the scan lines. Brightness temperature changes not due to the incident angle effect are, therefore, best interpreted along vertical columns from the top to the bottom of the image. The gradual brightness temperature change of the background (along a column) is attributed to gradual change in depth of snow and percentage of snow cover.

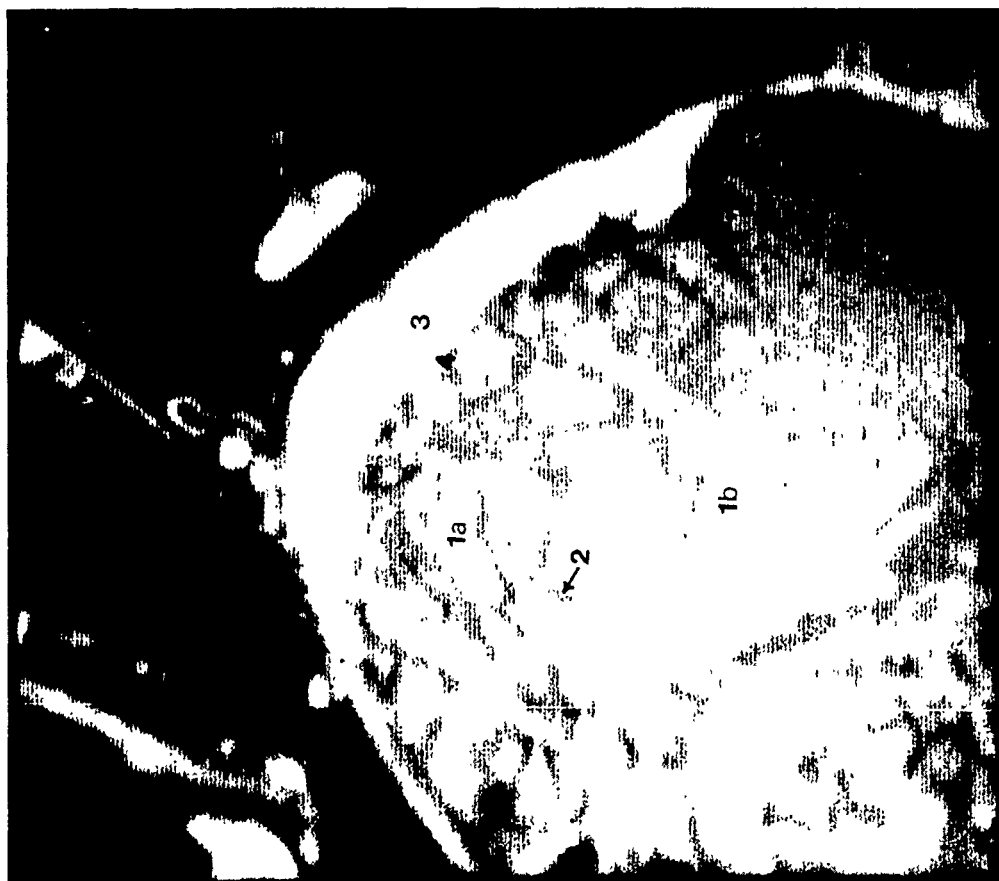
Type 2

The dark, linear features on the 8 March KRMS image correspond to the linear snow ice features observed in the field. These dark-toned, or radiometrically warm, materials correspond to the only linear features apparent on the aerial video. The linear features are light toned on the video and thus high visible albedo surfaces that would correspond to snow or snow ice. The only high albedo surfaces observed while traversing the lake were snow and snow ice and the only linear high albedo surfaces observed were the linear snow ice features (Fig. 7).

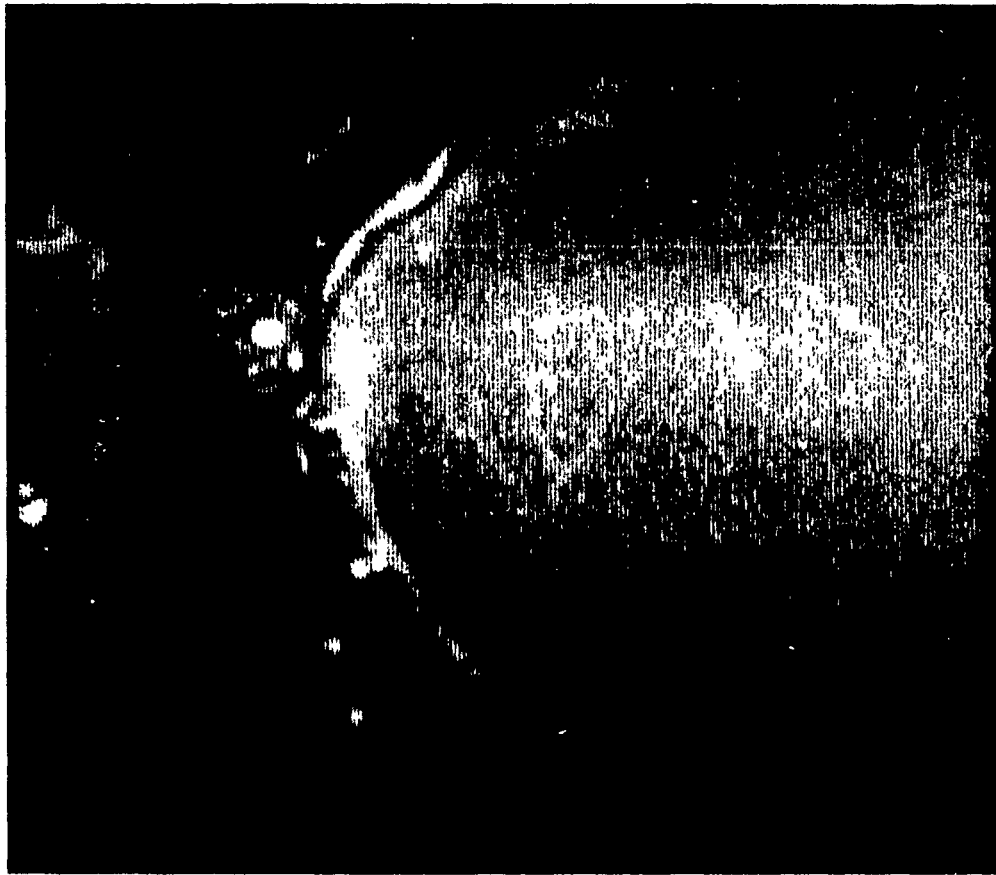
The number and arrangement of the linear features on the KRMS image suggest that they originated over fractures in the ice cover through which water seeped and wetted the overlying and nearby snow, forming a slush that later refroze into a white snow ice. Dark toned (radiometrically warm) areas adjacent to the frozen shelf on the northwest end of the lake are thought to be of similar origin. That is, cracks along the contact between floating and grounded ice flooded the snow cover above them, creating a localized surface layer of snow ice. Similar linear patterns seen on KRMS images of nearby Quartz and Birch lakes suggest that fracturing and localized snow ice formation also occurred there (Fig. 13). On all three lakes the linear patterns show up well on part of the surface where the background temperatures are low in contrast. The cooler background suggests deeper snow deposited in downwind areas. The weight of wind-blown snow may have depressed the ice surface to the hydrostatic water level and enhanced either the recognition of or the actual fracturing there.

Type 3

The wide radiometrically cold (light) band along the northwest shoreline corresponds to a shallow shelf where the ice was frozen to the bed. The band also corresponds to an area of the deepest and most continuous snow cover on the lake surface.



a. 8 March.



b. 11 March.

Figure 12. Equivalently scaled KRMS images 1. Mixed snow dunes and black ice with a) more snow, b) less snow; 2. linear snow ice features forming fracture patterns, 3. continuous, deep snow-cover over the shelf, 4. boundary zone between grounded and floating ice.



Figure 13. KRMS images (8 March) of Birch (left) and Quartz (right) lakes.

Radiometric explanations for image tones and patterns

Comparison of 8 and 11 March images

The overall darkening (increased radiometric temperature) observed on the 11 March KRMS image, as compared to the 8 March image, corresponds to increased emission from the snow, which had become wet by 11 March. Approximate KRMS brightness temperatures of the three surface types were sampled; averages are compared in Table 2.

The wet snow on the 11 March image effectively masks features that were distinguishable on 8 March when the snow was dry. As snow wetness increases, absorption becomes the dominant loss mechanism and penetration depth in the snow rapidly decreases (Hallikainen et al. 1984, Ulaby 1986). Calculations of the variation of penetration depth with liquid water content of snow are provided by Ulaby et al. (1986), for a range of frequencies, as shown on Figure 14. Experimental measurements showing increased brightness

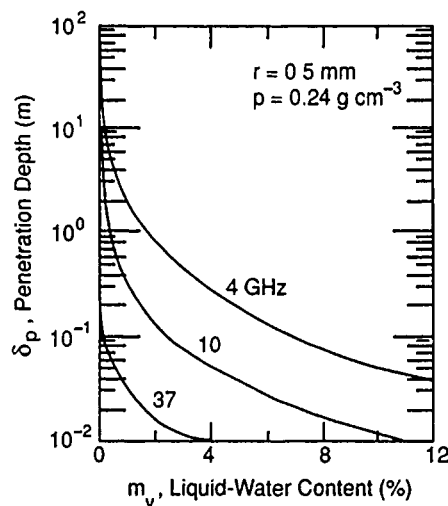


Figure 14. Variation of snow penetration depth with liquid water content (from Ulaby et al. 1986).

Table 2. KRMS radiometric temperatures (K) near nadir.

	8 March	11 March	Difference
Type 1—Background	204	229	25
Type 2—Linear snow-ice	224	229	5
Type 3—Shelf	184	226	42

temperature with increased volumetric water content are presented by Abdel-azik (1984) for volumetric water contents of 0% and 2% in a 50-cm snowpack (Fig. 15). Thus, it appears that decreased penetration depth due to wetness effectively masks the underlying ice or ground features on Harding Lake for wavelengths in the 33.6-GHz range because emissions by the underlying materials are absorbed in the wet snow layer. The wet snow layer itself would be highly emissive, resulting in the observed increased brightness temperature.

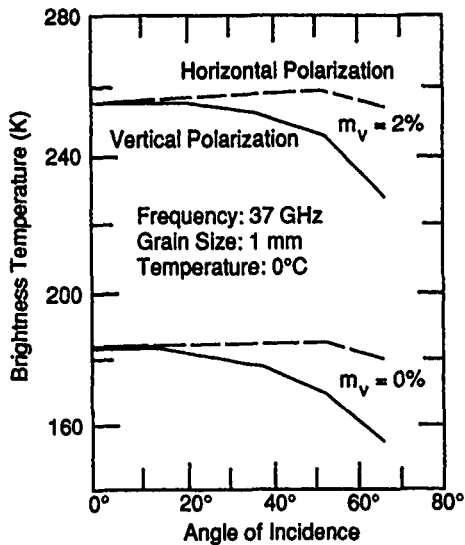


Figure 15. Calculated brightness temperature of snow-covered terrain for volumetric water contents of 0% and 2%, for a snow cover of 50 cm (from Abdelrazik 1984).

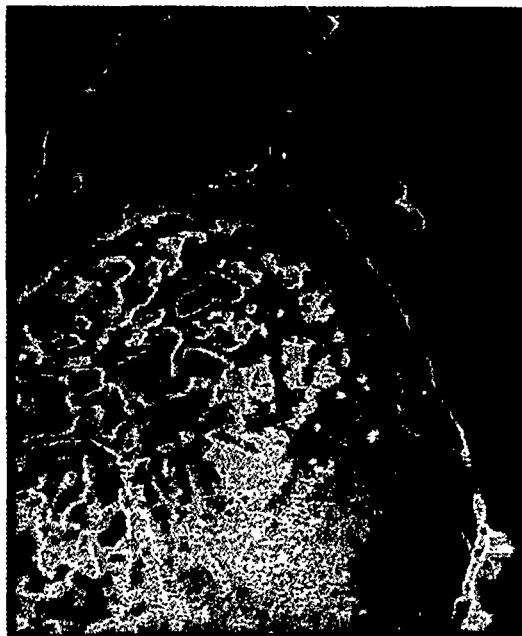


Figure 16. Color density slices of 8 March (left) and 11 March (right) images show the change in approximate brightness temperature. Colors are in 10 K intervals (see Table 3).

Gradual tonal changes in background

Gradual tonal changes in the background surface type in the 8 March image appear to result from variation in dry snow conditions across the lake. Variation in the percentage of snow cover is observed on the aerial video mosaic and suggests spatial variation in snow depth as well. The radiometric temperature of the background

Table 3. Scaled KRMS temperatures and color assignments.

Color	DV	Temp. (K)
Burgundy	42-57	265-256
Red	58-73	255-247
Pink	74-89	246-237
Orange	90-105	236-227
Yellow	106-121	226-217
Lt Yellow	122-137	216-208
Green	138-153	207-198
Cyan	154-169	197-188
Sky blue	170-185	187-178
Blue	186-201	177-169
Dk Blue	202-217	168-159
Lt Purple	218-233	158-149

type, observed along a vertical column near nadir, varies across two color divisions (light yellow and green), or roughly 20 K in brightness temperature (Fig. 16, Table 3). The radiometrically colder areas of the background type correspond to zones of more continuous snow cover on the video mosaic; the radiometrically warmer areas correspond to zones of discrete snow dunes interspersed with surfaces of snow-free black ice.

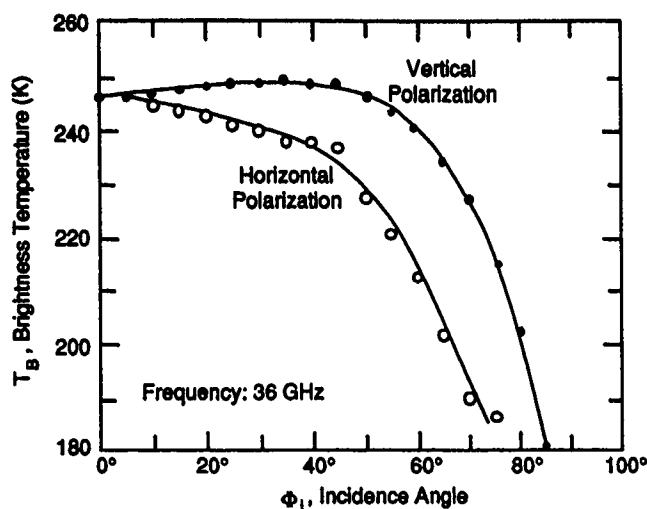


Figure 17. Brightness temperature of a wind drift type snow of 62-cm depth and 14-cm water equivalent (Shiue et al. 1978).

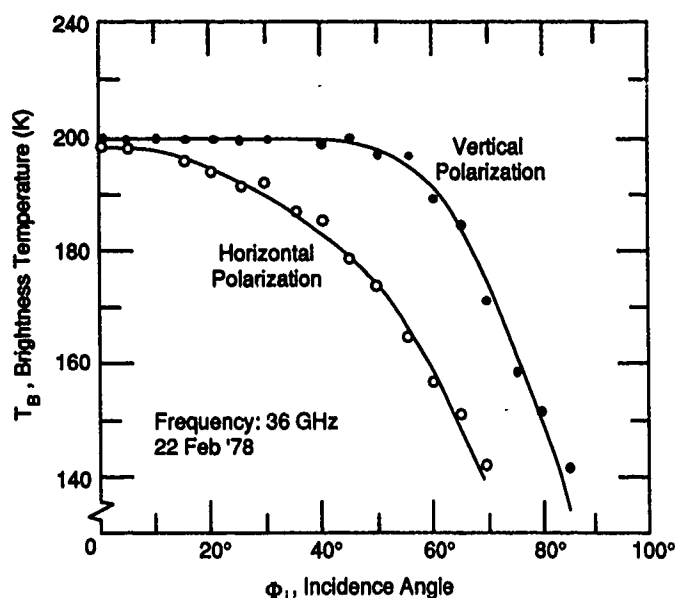


Figure 18. Brightness temperature of a depth hoar type snow of 59-cm depth and 14.2-cm water equivalent (Shiue et al. 1978).

Volume scattering, caused by dielectric discontinuities between air and ice crystals, is the dominant loss mechanism in dry snow (Hallikainen et al. 1984). Scattering increases as the number of scatterers increase; thus, with all else the same, deeper snow scatters more energy than thin snow. Scattering also increases as grain size increases relative to the wavelength. The effect of grain size on brightness temperature of wind drift and depth hoar type snowpacks, measured by Shiue et al. (1978) at 35 GHz over soil, show large temperature differences between the two types, with the small-grained snow

being much warmer than the coarse-grained snow (Fig. 17 and 18). Substantial scattering in the coarse-grained depth hoar on the lake surface probably decreases brightness temperatures over snow-covered ice relative to snow-free ice. The result is lower brightness temperatures in areas with more continuous and deeper snow cover.

Temperature gradients in the snow over the floating ice may have contributed slightly to the gradual changes in brightness temperature observed across the background surface type. By late afternoon on 8 March, temperatures in deeper and more continuous snow covers may have been a few degrees colder than in thinner and less continuous snowcovers or bare ice. The contribution to brightness temperature gradation would, however, be minor compared to the roughly 20 K range observed.

Linear feature contrast with background

The contrast of the linear snow ice features with the background type is probably due to less scatter in the snow ice layer than in the snow cover over the adjacent ice surface. The change in approximate brightness temperature of the linear snow ice features between the two flight dates is minimal, only 5 K warmer on the second date (Table 2). In comparison, the approximate change in brightness temperature of the adjacent snow-covered background type was around 25 K, and the change in radiometric temperature of the shelf was around 42 K. The relative increase in brightness temperature is due to the change in snow wetness between the two flight dates; areas with more continuous snow cover were more significantly affected.

Shelf area

The shelf area where ice is frozen to the bed appears as a striking white band across the north-west end of the lake on the 8 March image. Because of the short wavelength (0.89 cm) it is doubtful that we are seeing a difference due to the shelf, but rather a condition coincident with the shelf. The ability to distinguish the shelf is thought to result from two factors: first, the shelf is covered with a deeper and more continuous snowpack than the open lake, which results in lower average brightness temperatures; and second, the shelf contrasts with the radiometrically warm zone bordering the lakeward edge of the shelf. As previously mentioned, fractures may have occurred at the lakeward margin of the grounded ice, flooding the snow cover above them and forming a radiometrically warm snow ice layer there.

Temperature gradients in the snowpack over the shelf may have contributed slightly to the relatively cold brightness temperatures observed there. The average temperature in the deeper and more continuous snow cover over the shelf may have been several degrees lower than in the thinner and less continuous snow cover over the floating ice. Brightness temperature contrasts between the shelf and background (20 K difference) and the shelf and linear snow ice features (40 K difference) are much greater than differences that could be attributed to snowpack temperature. These brightness temperature contrasts are thus thought to primarily result from scattering in the thick depth hoar layer.

CONCLUSIONS

We were able to distinguish three surface types on the lake: 1) a mixture of snow dunes interspersed with snow-free black ice, 2) the linear snow ice features revealing a fracture pattern, and 3) snow-covered grounded ice. The radiometric contrast between them appears to result from relative differences in scattering by the surface materials. The linear snow ice along and above the fractures had fewer large scatterers, resulting in the radiometrically warmest areas (dark on 8 March) on the lake surface. Depth hoar crystals in the snow dunes are thought to be the source of significant scattering, resulting in a radiometrically cool (medium to light-toned) background, varying in tone with the relative amount of snow-free ice and with snow depth. The deepest and most continuous snow occurs over the shelf and causes the most scatter, resulting in the coldest signature (lightest) on the lake. The ability to distinguish the grounded ice from floating ice is attributed to the deeper and more continuous snow cover over the shelf, not the shelf itself being sensed. The delineation of the lakeward margin of the grounded ice is an interpretation based on radiometric contrast of the snow-covered shelf with warmer snow ice formed over fractures at the boundary between the floating and grounded ice. Temperature gradients in the snowpack may contribute slightly to the lower radiometric temperatures from areas of deeper and more continuous snow cover; however, scattering in the depth hoar is believed to be the dominant cause.

Low altitude passive microwave imagery is a promising method for remote/field investigation of lake ice processes, especially the occurrence, extent and density of large-scale fracturing of a lake ice surface. KRMS images of nearby Birch and Quartz lakes displayed linear features much like those on Harding Lake, suggesting that similar fracturing and water seepage into the surface snow had occurred on these similarly sized lakes. Additional field verifications are needed to show what range of snow and ice conditions allow observation

of the fracture patterns. The surface expressions of the fractures on Harding Lake were linear snow ice features that contrasted with radiometrically colder depth-hoar-covered ice. Our lake site was a subarctic region of cold winters and moderate snowfall; it may be inappropriate to assume that similar patterns observed in climate regions that do not create shallow, highly metamorphosed snowpacks are due to the same set of circumstances. In addition, the fractures may not be detectable during years when subsequent snowfall buries the snow ice features.

LITERATURE CITED

- Abdelrazik, M. (1984) The dielectric behavior of snow in the 3- to 37-GHz range. PhD thesis (unpublished), University of Kansas.
- Arcone, S.A. and A.J. Delaney (1987) Airborne river-ice thickness profiling with helicopter-borne UHF short-pulse radar. *Journal of Glaciology*, 33(115): 330-340.
- Eppler, D.T., L.D. Farmer and A.W. Lohanick (1984) Digital processing of passive K_a-band microwave images for sea-ice classification. Naval Ocean Research and Development Activity, NSTL, Mississippi, Report 51.
- Eppler, D.T. and B. Heydlauf (in press) Digitizing analog KRMS data on a personal computer. Naval Ocean Research and Development Activity, Stennis Space Center, Mississippi, Technical Report 219.
- Farmer, L.D., D.T. Eppler and A.W. Lohanick (1990) Converting digital passive microwave data to kelvin units of brightness temperature. Naval Ocean Research and Development Activity, Stennis Space Center, Mississippi, Technical Note 427.
- Gloersen, P. and F.T. Barath (1977) The Seasat-A scanning multichannel microwave radiometer. *IEEE Journal of Oceanic Engineering*, V(OE-2): 172-178.
- Gow, A.J. (1986) Orientation textures in ice sheets of quietly frozen lakes. *Journal of Crystal Growth*, 74: 247-258.
- Gray, D.M. and D.H. Male (Ed.) (1981) Handbook of snow: Principles, processes, management and use. In *Snow and Ice on Lakes* by W.P. Adams. Toronto: Pergamon Press Canada Ltd., Chapter 10, p. 437-474.
- Hall, D.K., J.L. Foster, A. Rango and A.T.C. Chang (1978) Passive microwave studies of frozen lakes. In *Proceedings of the American Society for Photogrammetry, Fall Technical Meeting, October 15-20, Albuquerque, New Mexico*, p. 195-208.
- Hall, D.K., J.L. Foster, A.T.C. Chang and A. Rango (1981) Freshwater ice thickness observations using passive microwave sensors. *IEEE/Transactions on Geoscience and Remote Sensing*, GE-19(4): 193.

- Hallikainen, M., F.T. Ulaby and M. Abdelrazik** (1984) The dielectric behavior of snow in the 3- to 37-GHz range. In *Remote Sensing From Research Towards Operational Use. International Geoscience and Remote Sensing Symposium (IGARSS '84), Strasbourg, August 27-30*. European Space Agency, ESA SP-236, vol. 2, p. 169-174.
- Haugen, R.K. and J. Brown** (1978) Climatic and dendroclimatic indices in the discontinuous permafrost zone of the central Alaskan uplands. In *Proceedings, 3rd International Conference on Permafrost, 10-13 July. Edmonton, Alberta*. Ottawa: National Research Council of Canada, p. 392-398.
- Knight, C.A.** (1962) Studies of arctic lake ice. *Journal of Glaciology*, 4: 319-335.
- Melloh, R.A. and L.W. Gatto** (1990a) Interpretation of passive and active microwave imagery over snow-covered lakes and rivers near Fairbanks, Alaska. In *Proceedings of the Applications of Remote Sensing in Hydrology, 13-14 February, Saskatoon, Saskatchewan*. National Hydrology Research Institute of Canada, p. 259-278.
- Melloh, R.A. and L.W. Gatto** (1990b) Interpretation of synthetic aperture radar imagery of snow-covered river ice. In *Proceedings of the USACE Seventh Remote Sensing Symposium, Portland, Oregon, 7-9 May*, p. 429-441.
- Nakao, K. (Ed.)** (1980) Climatic changes in interior Alaska. Report of the Alaskan Paleolimnology Research Project-1977/78/79. Laboratory of Hydrology, Department of Geophysics, Hokkaido University.
- NOAA** (1989) Climatological Data Records for February and March 1988. National Oceanic and Atmospheric Administration, Washington, D.C.
- Reeves, R.G. (Ed.)** (1975) *Manual of Remote Sensing*. Falls Church, Virginia: American Society of Photogrammetry.
- Schmugge, T., T.T. Wilheit, P. Gloersen, M.F. Meir, D. Frank and I. Dormhirn** (1973) Microwave signatures of snow and freshwater ice. In *Advanced Concepts and Techniques in the Study of Snow and Ice Resources*. Washington, D.C.: National Academy of Sciences, p. 551-562.
- Shaw, J.B.** (1965) Growth and decay of lake ice in the vicinity of Schefferville, Quebec. *Arctic*, 18(2): 123-132.
- Shiue, J.C., A.T.C. Chang, H. Boyne and D. Ellerbruch** (1978) Remote sensing of snowpack with microwave radiometers for hydrologic applications. In *Proceedings of the 12th International Symposium on the Remote Sensing of the Environment, Ann Arbor, Michigan*, p. 887-896.
- Svendsen, E., K. Kloster, B. Farrelly, O.M. Johannessen, J.A. Johannessen, W.J. Campbell, P. Gloersen, D.J. Cavalieri and C. Matzler** (1983) Norwegian remote sensing experiment: Evaluation of the Nimbus 7 scanning multichannel microwave radiometer for sea ice research. *Journal of Geophysical Research*, 88(C5): 2781-2791.
- Swift, C.T., L.S. Fedar and R.O. Ramseier** (1985) An algorithm to measure sea ice concentration with microwave radiometers. *Journal of Geophysical Research*, 90(C1): 1087-1099.
- Ulaby, F.T., R.K. Moore, and A.K. Fung** (1986) *Microwave Remote Sensing—Active and Passive*. Reading, Massachusetts: Addison-Wesley Publishing Company, Inc, vol. III, p. 1607-1612.

APPENDIX A: KRMS DESCRIPTION.

Scan geometry

KRMS senses microwave emissions from the earth's surface through three parabolic antennas (Fig. A1). The three antennas, mounted 120° apart on a single shaft, rotate about a horizontal axis that is parallel to the direction of flight and scan in a vertical plane (Fig. A2). As the antenna assembly rotates an electronic switch enacts so that only the signal from the downward-facing antenna is recorded. During each rotation each antenna in turn scans a 120° field-of-view centered at aircraft nadir, of which the central 100° is digitized. Three scan lines are thus recorded for each rotation. The ground swath, or image width across this 100° field, is equal to 2.38 times the height of the aircraft above ground.

Downtrack (forward) motion of the aircraft moves the position of the scanning swath further along track, and an image is built simply by recording successive scans. An operator in the aircraft manually adjusts the rate at which the antenna assembly rotates both to ensure a nominal overlap of 80% (at nadir) between successive scans and to preserve correct image geometry in the downtrack direction. Overlap at off-nadir angles is greater than 80% because the size of the beamspot increases with incidence angle (Fig. A3). Increased ground speed or decreased altitude require increased rotation rate to maintain constant scan-to-scan overlap. Rotation rate can be adjusted to acquire between 7 and 25 scans of the ground per second, which permits continuous coverage at altitudes above 305 m.

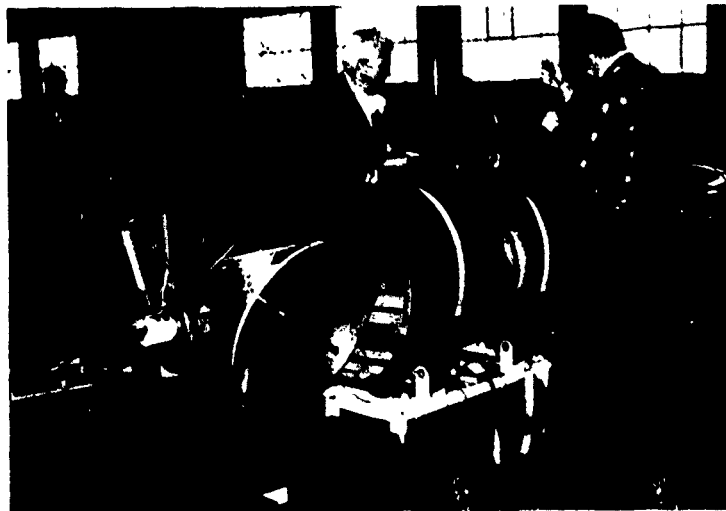


Figure A1. The KRMS antenna assembly. (Photograph by D. Farmer, December 1981.)

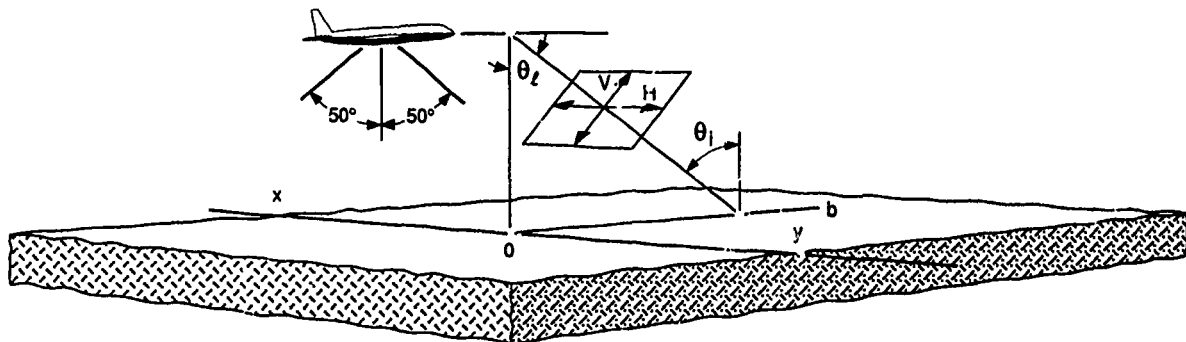


Figure A2. Scan geometry of KRMS antennas. Measured radiation is vertically polarized at all off-nadir angles (from Eppler et al. 1984). θ_l = look angle. θ_i = incidence angle.

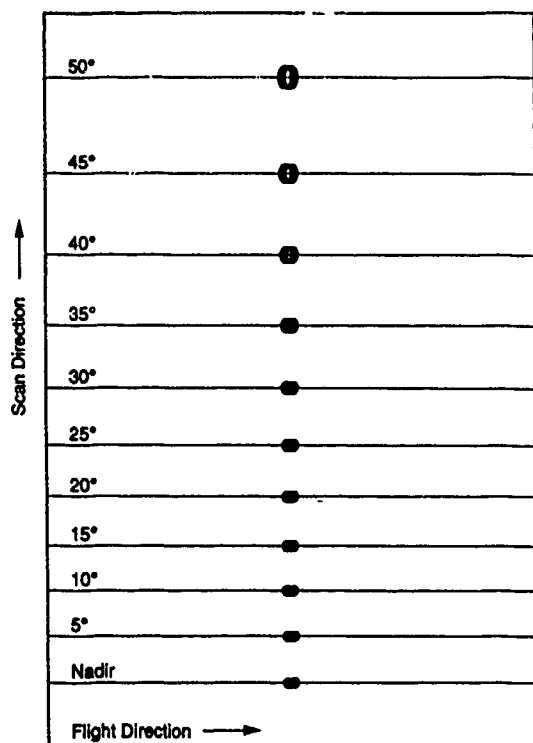


Figure A3. Overlap between beams in adjacent KRMS scans plotted for different incidence angles.

Thermal sensitivity and spatial averaging

KRMS's minimum detectable signal as measured in the laboratory is 0.05 K per second; operational sensitivity is believed to be 0.5 K or better. Antenna beam width is 1°, which subtends a circular beamspot on the ground at nadir that is approximately 5.7 m in diameter per 305 m of flight altitude. At off-nadir angles the beam subtends a larger spot that is elliptical; both size and ellipticity increase with increasing off-nadir angle (Fig. A4). Image detail near the edges of KRMS images may appear blurred as a result of beam spreading, whereas optimal spatial and radiometric resolutions are achieved near nadir.

Qualitative observations made in the process of analyzing sea ice imagery demonstrate that both the size of a particular feature and its radiometric contrast with respect to adjacent features determine whether it can be resolved by the KRMS. For example, cracks in first-year sea ice much narrower than the KRMS beamspot produce distinct signatures on KRMS images because the cracks expose radiometrically cold water that contrasts sharply with adjacent radiometrically warm first-year ice. On the other hand, large features visible in airphotos

50°	0.9008	3.7659
45°	0.6767	2.8288
40°	0.5322	2.2247
35°	0.4352	1.8194
30°	0.3683	1.5397
25°	0.3213	1.3433
20°	0.2883	1.2052
15°	0.2654	1.1096
10°	0.2505	1.0470
5°	0.2420	1.0015
Nadir	0.2392	1.000

Figure A4. Variations in the size and ellipticity of the KRMS 3-dB beamspot as a function of incidence angle. Two conversion factors are given for each angle. The left number, when multiplied by a reference aircraft altitude, gives the area of the beamspot in square units of altitude. The area subtended by the nadir beamspot from 3,000-m altitude thus is 718 m². The right number represents the relative area of the beamspot with respect to the area of the nadir beamspot. The area imaged by each beam at 50° thus is 3.7659 times larger than the area imaged at nadir.

may be far less distinct in KRMS images or not detectable at all because of poor radiometric contrast with adjacent materials.

Data Processing

KRMS images are recorded in real time on analog tape aboard the aircraft. Upon completion of a flight, the analog tapes are converted to digital 9-track computer compatible tapes (Eppler and Heydlauf 1990). Differences in response characteristics of KRMS's three antennas are minimized by adjusting gains and offsets applied to the analog signal as it is digitized. Pixel radiances are recorded as short unsigned integers that range in digital value from 0 to 2047. These can be converted to radiometric temperatures according to methods described by Farmer et al. (1990).

Temperature scaling

The KRMS data can be approximately calibrated using targets of known brightness temperature within the imaged scene and reference load voltages recorded in flight along with the analog record (Farmer et al. 1990). The method used to convert digital values to brightness temperatures consisted of estimating brightness temperatures corresponding to the low (0) and high (2047) digital values and linearly scaling all intermediate values. The high digital count (2047) for both flight dates was set to correspond to imaged areas of open water near nadir and was assigned a brightness temperature of 135 K, calculated for the Fresnel reflection coefficients for saline water at 33.6 GHz. The low digital count was set at reference load temperatures for the 8 and 11 March flights of 291 K and 270 K, respectively.

Atmospheric, cosmic and instrument related contributions are included (as seen below) in the reference load temperature but not the brightness temperature of open water, the former being measured at the antenna and the latter being an assigned brightness temperature at the water surface. As a result, the calibration line slope is greater than would be a conversion to actual brightness temperature. The magnitude of atmospheric and cosmic contributions and the difference in the magnitude of these contributions from one flight date to the next were estimated, and are summarized below. We show that these contributions are small and did not change between flights. We also assume that instrument-related errors did not change significantly between the two flights (Farmer et al. 1990). Differences in image tone and pattern from one image to the next (8 to 11 March), which are far larger than the estimated error in calibration methods, can be attributed to changes in emissivity or scattering by the surface between the two dates.

Apparent temperature contributions

The brightness temperature of a surface material is expressed as the physical temperature T_0 of the object times its emissivity:

$$T_B = E T_0 \quad (A1)$$

where emissivity of the surface material E is simply the ability of a surface to emit or absorb radiation. Microwave energy incident on the antenna of a passive sensor looking through an atmosphere, however, comes not only from emission by the surface materials, but from the atmosphere and cosmic sources as well. Methods devised to treat passive microwave data retrieved from satellite sensors provide a basis for estimating the magnitude of energy attributed to these sources (Gloersen and Barath 1977, Svendsen et al. 1983, Swift et al. 1985).

The raw, composite radiance or apparent temperature (T_A) sensed by KRMS can be described by

$$T_A = E T_0 e^{-\alpha} + T_{ATM} + (1 - E) T_{ATM} e^{-\alpha} + (1 - E) T_{SP} e^{-(\alpha+\beta)} \quad (A2)$$

where T_0 = the physical temperature of the surface material

α = opacity of the atmosphere between KRMS and the surface

β = opacity of the total atmosphere,

T_{ATM} = physical temperature of the atmosphere (upwelling in term 2 and downwelling in term 3)

T_{SP} = 2.7 K, the physical temperature of cosmic background radiation from space.

Equation A2 was adapted from Swift et al. (1985). The first term is the brightness temperature, corrected for attenuation by the atmosphere (Fig. A5). The second term represents upwelling atmospheric radiation. The third term is downwelling atmospheric radiation reflected from the surface and attenuated by the atmosphere between the surface and the sensor. The fourth term accounts for cosmic radiation from space that is attenuated by the atmosphere, first along its downward path from the top of the atmosphere to the surface, and then again along its upward path to the sensor after reflection from the surface.

Table A1 gives estimates of atmospheric opacity (τ) during winter in high latitudes. Values for τ were calculated by Svendsen et al. (1983) on the basis of work summarized in Reeves (1975). In eq A2, we use the notation β for τ ; β corresponds to the opacity of the entire atmospheric column. Values for α (atmospheric opacity below the aircraft) were derived by reducing β by the percentage of the total atmospheric column that occurs between KRMS and the surface. This ratio method assumes that the composition of the arctic atmosphere was vertically homogeneous at flying altitudes with respect to constituents that cause attenuation (oxygen and water vapor). All data described in this report were

Table A1. Atmospheric opacities for subarctic winter (from Svendsen et al. 1983).

	Frequency (GHz)				
	6.6	10.7	18	21	37
Oxygen	0.011	0.011	0.015	0.022	0.034
Water vapor	0.000	0.001	0.006	0.016	0.012
Liquid water	0.001	0.003	0.009	0.012	0.038
Total zenith	0.012	0.015	0.030	0.050	0.084
Total 50°	0.019	0.023	0.047	0.078	0.0130

Air temperature = 270 K.

Water vapor = 0.4 cm.

Liquid water = 0.02 cm

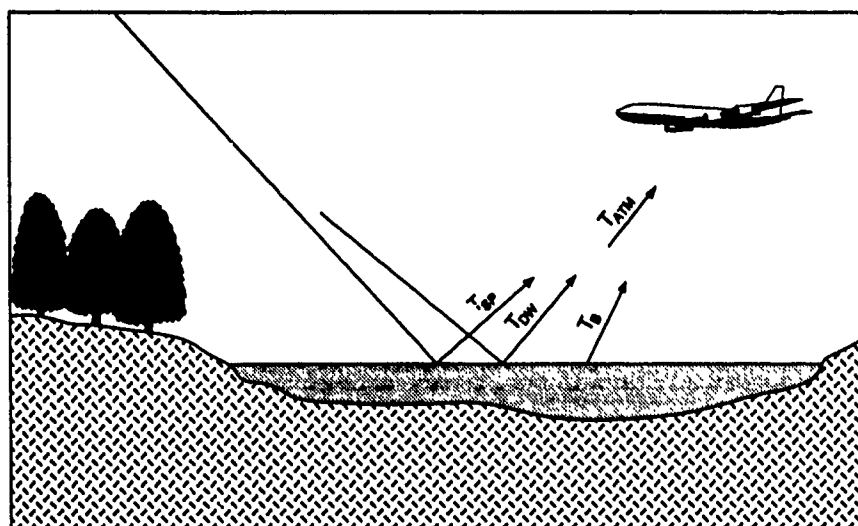


Figure A5. Apparent temperature contributions. Energy emitted from the surface (T_B), upwelling atmospheric radiation (T_{ATM}), and reflected downwelling atmospheric (T_{DW}) and cosmic (T_{SP}) radiation.

acquired from 1500 m above sea level; using a standard atmosphere we calculate that 19% of the atmosphere lies below this altitude.

Swift et al. (1985) show that T_{ATM} of eq A2 is approximated by

$$T_{ATM} = T_M(1 - e^{-\tau}). \quad (A3)$$

T_M is the mean temperature of the atmospheric column and can be expressed as a function of surface temperature (T_S) and adiabatic lapse rate

$$T_M = 1.12 T_S - 50. \quad (A4)$$

Atmospheric attenuation

The first term of eq A2 accounts for the brightness temperature of the surface material attenuated by the atmosphere between the surface and KRMS. Adopting a τ at 33.6 GHz of 0.077 from interpolation between Svendsen's data (Table A1) for a subarctic winter atmosphere gives an α of 0.015. The estimated air temperatures at Harding Lake were 272 K and 278 K, during the March 8 and 11 flights. The physical temperatures of the surface snow and ice (T_0) were estimated to be 272 K for both dates. Calculated attenuation of brightness temperatures were on the order of 2 to 4 K for emissivities of 0.5 to 0.95, respectively.

Upwelling atmospheric component

The second term of eq A2 accounts for energy upwelling from the atmosphere below the sensor. Haugen and Brown (1978) compiled typical seasonal air temperature profiles for Fairbanks, Alaska, for elevations between 0 and 3000 m; April curves show a uniform elevational gradient of 1°C per 100 m, above 500 m above sea level. Estimated by eq A3, contributions of

upwelling atmospheric energy (T_{ATM}) from below 1500 m, for a wide range of possible mean atmospheric temperatures for the two flight dates, were around 4 K.

Reflected downwelling atmospheric and cosmic components

The third and fourth terms of eq A2 account for downwelling atmospheric and cosmic radiation (2.7 K) reflected from the surface. The downwelling atmospheric component was estimated by eq A3 and A4 to be 19 K for both flight dates. The magnitude of the reflected energies depends on emissivity (E) which varies with surface materials and ranges approximately from 0.5 for water to 0.94 for highly emissive first-year sea ice and 1.0 for a perfect blackbody. The magnitude of reflected downwelling radiation sensed by KRMS thus depends on physical characteristics of surfaces imaged in each beamspot and varies from point to point in a scene. Contributions for a range of emissivities (0.5 to 1.0) are shown on Table A2. Reflected contributions are minimal over highly emissive surfaces, thus contributing little to radiometric temperatures of the warm tie point which is measured at the KRMS antenna.

Table A2. Reflected downwelling atmospheric and cosmic contributions to apparent temperature.

Surface emissivity (E)	Downwelling atmosphere (K)	Cosmic radiation (K)
0.5	9.4	1.2
0.6	7.5	1.0
0.7	5.6	0.7
0.8	3.7	0.5
0.9	1.9	0.25
1.0	0.0	0.0

APPENDIX B: ICE CORES.

Ice cores taken at locations along the transect (Fig. 6) consist stratigraphically of granular ice on top and either columnar or macrocrystalline ice below (Fig. B1). Transitions from granular to columnar or massive forms are noticeable on 1.9-cm-thick samples of the ice (Fig. B2a, B4a, B10a, B16a, B17a and B18a) and thin sections prepared from the ice samples (Fig. B2b, B4b, B10b, B16b, B17b, and B18b). The thin sections are less than

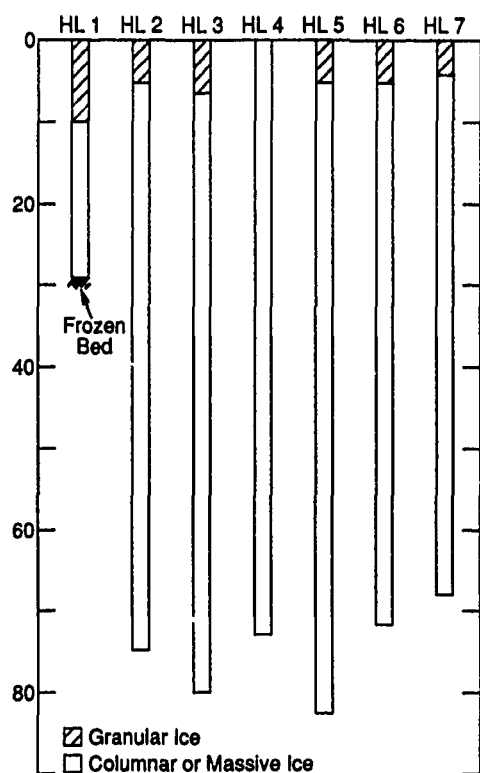


Figure B1. Composition of ice cores.

0.05 cm in thickness; this allows individual crystals to be seen when the ice is inserted between cross-polarized sheets.

Granular ice at the top of the cores was likely to have formed when the snow cover on the ice was flooded by lake water or radiatively melted, and later refrozen. A thicker granular ice stratum composed of layers of grains of differing sizes suggests either separate episodes of granular ice formation over the shelf or more snow layers (Fig. B2b). Some possibilities are that a wind-driven current accumulated frazil or snow slush over the shelf prior to freeze-up, or that an ice cover formed earlier in the shallow zone and episodes of windblown snow or snowfall were followed by melt or flooding.

Ice crystals that were formed from direct freezing of lake water make up the remainder of the ice cores. Distinctly outlined, columnar crystals with horizontal c-axes were sometimes found just beneath the granular ice; examples of these are seen in Fig. B17b. The limited occurrence of columnar crystals may indicate the lake surface froze under relatively quiet conditions without significant meteorological seeding, according to recent work by Gow (1986). Large, irregularly shaped and striated crystals with vertical c-axis orientation predominate lower in the ice cores (examples in Fig. B4b and B11b). Sinuous striations (Fig. B6b, B7b, B12b, B14b, and B15b) occur in the macrocrystalline ice; these have been observed previously in arctic lake ice and are attributed to misalignments in sub-grain structure (Knight 1962). We do not know what environmental factors caused the sinuous striations in the ice of Harding Lake.

Vertically elongated tubular bubbles in the lake ice were generally less than 5 cm in length and 1 to 3 mm in diameter. Clear bubbles are air filled (Fig. B3a) while bubbles that appear dark in the photographs were filled with small ice crystals and air bubbles (Fig. B8a).

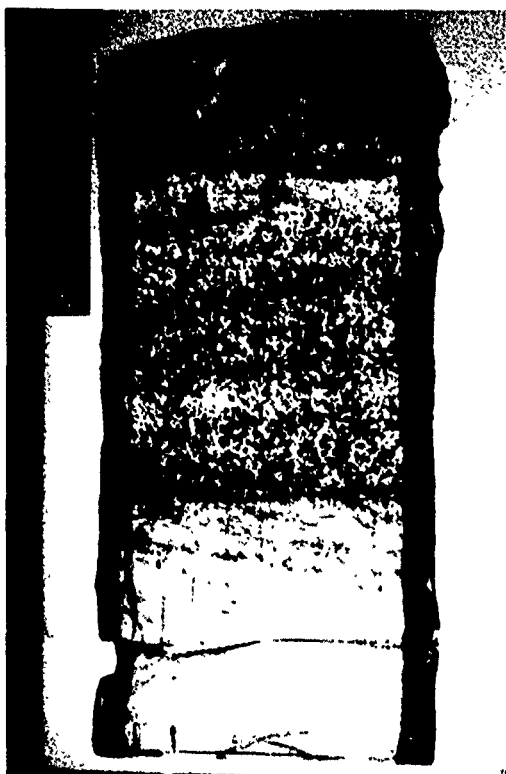


Figure B2a. Core HL1, 0-15 cm, thick section.



Figure B2b. Core HL1, 0-15 cm, thin section.



Figure B3a. Core HL1, 16-30 cm, thick section.



Figure B3b. Core HL1, 16-30 cm, thin section.



Figure B4a. Core HL2, 0-15 cm, thick section.



Figure B4b. Core HL2, 0-15 cm, thin section.



Figure B5a. Core HL2, 15-25.5 cm, thick section.



Figure B5b. Core HL2, 15-25.5 cm, thin section.



Figure B6a. Core HL2, 27-14.5 cm, thick section.



Figure B6b. Core HL2, 27-14.5 cm, thin section.



Figure B7a. Core HL2, 42-57 cm, thick section.

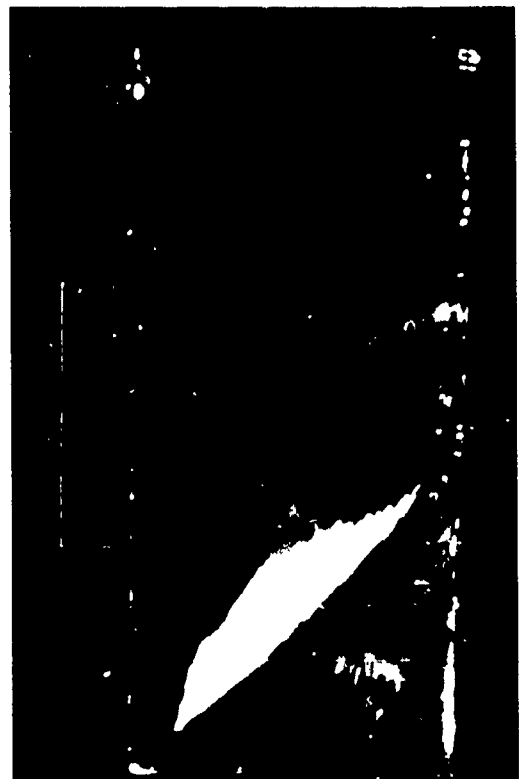


Figure B7b. Core HL2, 42-57 cm, thin section.



Figure B8a. Core HL2, 57.5–71.5 cm, thick section.

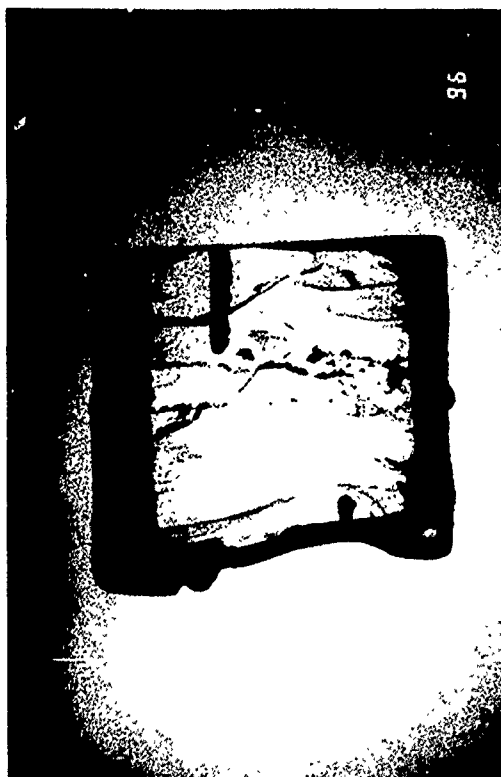


Figure B9a. Core HL2, 72–79 cm, thick section.

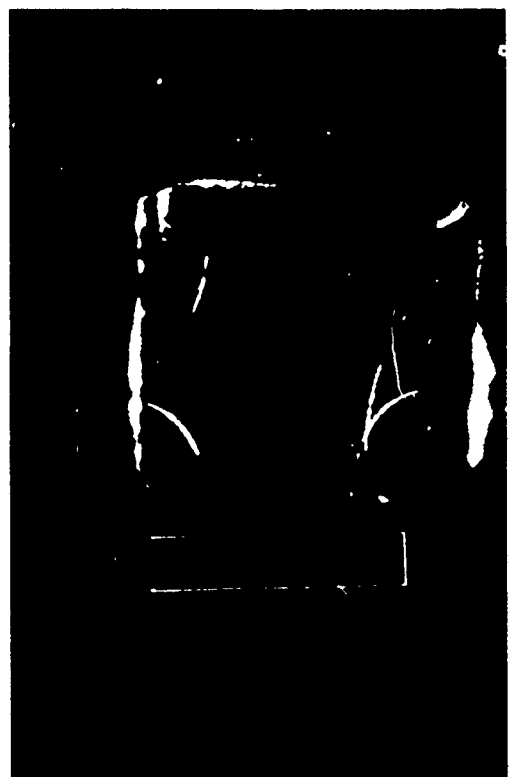


Figure B9b. Core HL2, 72–79 cm, thin section.

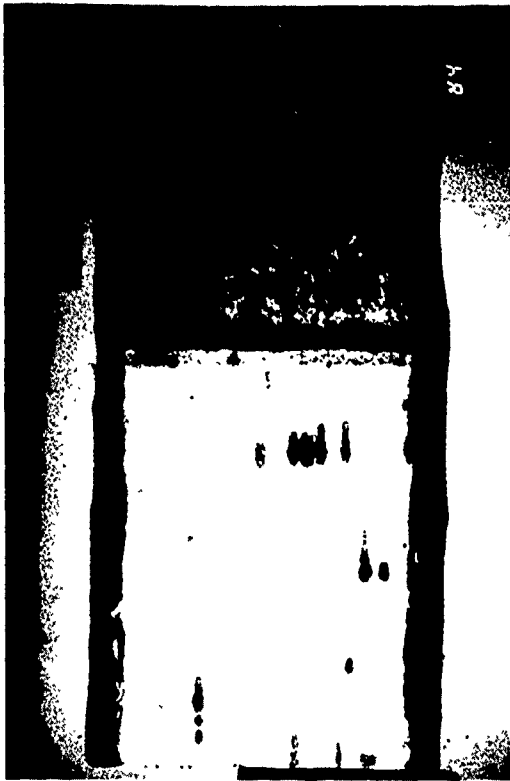


Figure B10a. Core HL3, 0-15 cm, thick section.



Figure B10b. Core HL3, 0-15 cm, thin section.



Figure B11a. Core HL4, 0-14 cm, thick section.



Figure B11b. Core HL4, 0-14 cm, thin section.

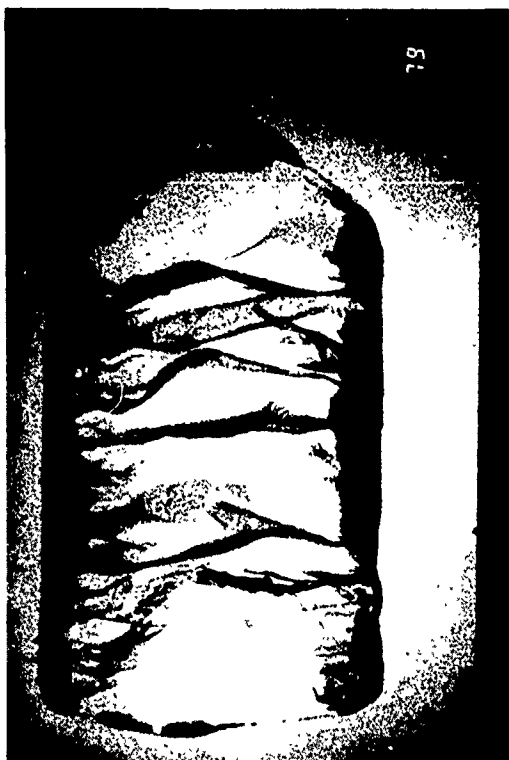


Figure B12a. Core HLA, 16-28 cm, thick section.



Figure B12b. Core HLA, 16-28 cm, thin section.



Figure B13a. Core HLA, 30-43 cm, thick section.



Figure B13b. Core HLA, 30-43 cm, thin section.

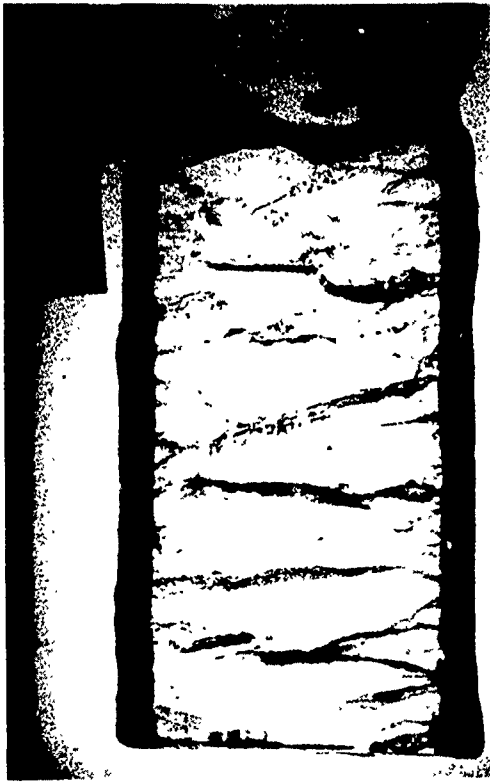


Figure B14a. Core HLA, 45-62.5 cm, thick section.

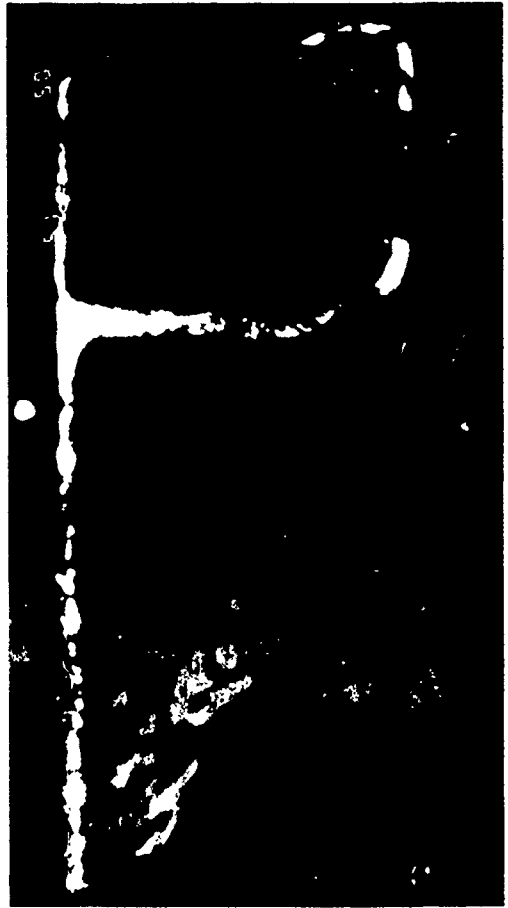


Figure B14b. Core HLA, 45-62.5 cm, thin section.



Figure B15a. Core HLA, 64-77 cm, thick section.

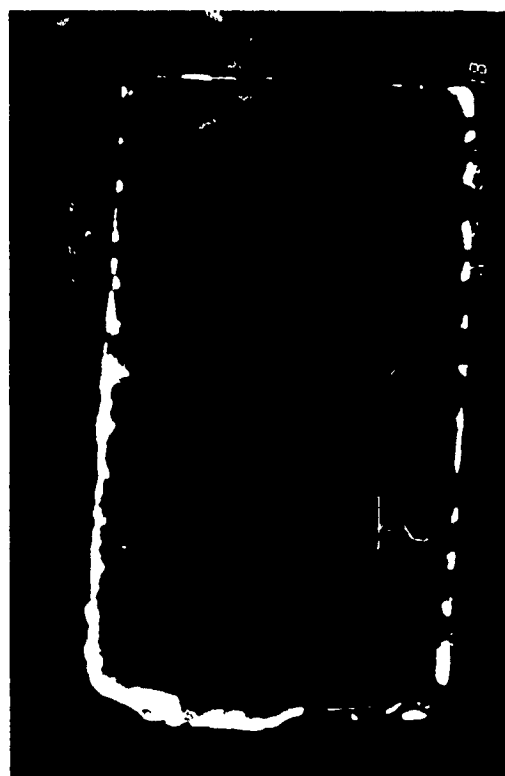


Figure B15b. Core HLA, 64-77 cm, thin section.

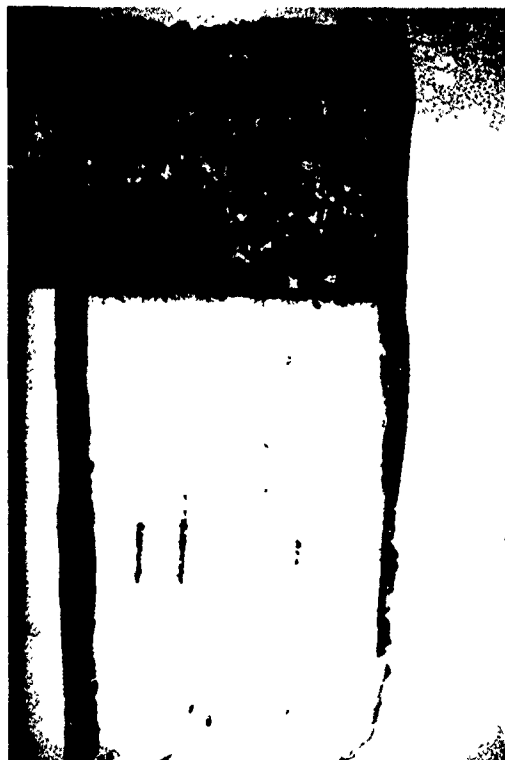


Figure B16a. Core HL5, 0-15 cm, thick section.



Figure B16b. Core HL5, 0-15 cm, thin section.

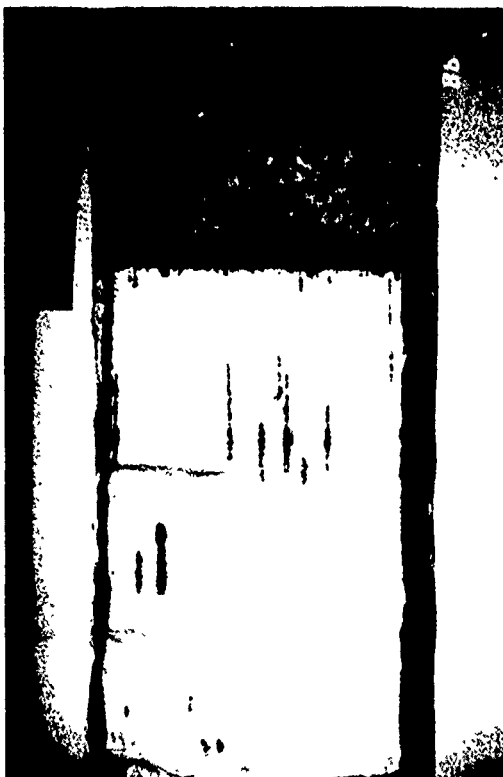


Figure B17a. Core HL6, 0-15 cm, thick section.



Figure B17b. Core HL6, 0-15 cm, thin section.

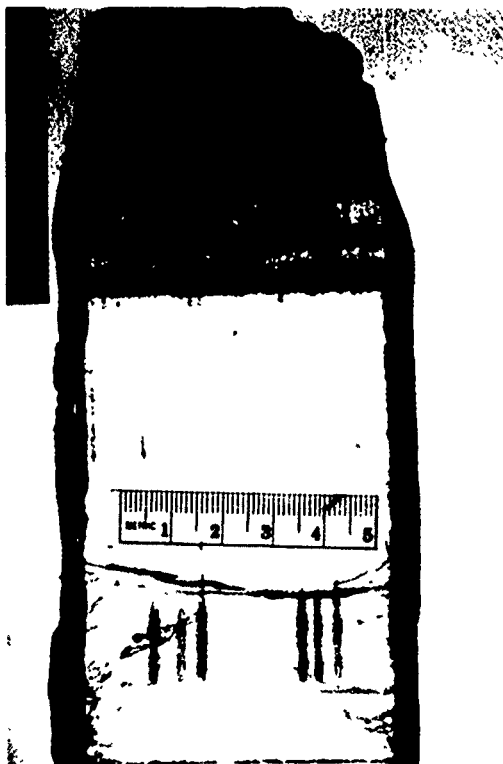


Figure B18a. Core HL7, 0-15 cm, thick section.



Figure B18b. Core HL7, 0-15 cm, thin section.

REPORT DOCUMENTATION PAGE

Form Approved
OMB No. 0704-0188

Public reporting burden for this collection of information is estimated to average 1 hour per response, including the time for reviewing instructions, searching existing data sources, gathering and maintaining the data needed, and completing and reviewing the collection of information. Send comments regarding this burden estimate or any other aspect of this collection of information, including suggestion for reducing this burden, to Washington Headquarters Services, Directorate for Information Operations and Reports, 1215 Jefferson Davis Highway, Suite 1204, Arlington, VA 22202-4302, and to the Office of Management and Budget, Paperwork Reduction Project (0704-0188), Washington, DC 20503.

1. AGENCY USE ONLY (Leave blank)		2. REPORT DATE June 1991		3. REPORT TYPE AND DATES COVERED	
4. TITLE AND SUBTITLE Interpretation of Passive Microwave Imagery of Surface Snow and Ice: Harding Lake, Alaska				5. FUNDING NUMBERS In-House Laboratory Independent Research Program, ILIR 499/500	
6. AUTHORS Rae A. Melloh, Duane T. Eppler, L. Dennis Farmer, Lawrence W. Gatto and Edward F. Chacho					
7. PERFORMING ORGANIZATION NAME(S) AND ADDRESS(ES) U.S. Army Cold Regions Research and Engineering Laboratory 72 Lyme Road Hanover, New Hampshire 03755-1290				8. PERFORMING ORGANIZATION REPORT NUMBER CRREL Report 91-11	
9. SPONSORING/MONITORING AGENCY NAME(S) AND ADDRESS(ES) U.S. Army Cold Regions Research and Engineering Laboratory 72 Lyme Road Hanover, New Hampshire 03755-1290				10. SPONSORING/MONITORING AGENCY REPORT NUMBER	
11. SUPPLEMENTARY NOTES					
12a. DISTRIBUTION/AVAILABILITY STATEMENT Approved for public release; distribution is unlimited. Available from NTIS, Springfield, Virginia 22161				12b. DISTRIBUTION CODE	
13. ABSTRACT (Maximum 200 words) This report presents interpretations of snow and ice conditions on Harding Lake, Alaska, using 33.6-GHz passive microwave imagery acquired from 1500 m on 8 and 11 March 1988, when snow conditions were dry and wet, respectively. Field data used include an aerial video mosaic, ice column descriptions, snow observations and an impulse radar trace. Our results show that low-altitude passive microwave imagery is a promising method for remote/field investigation of large-scale lake ice processes. Fracture patterns in the lake ice were detected where snow ice had formed above and near cracks in the ice cover. Presumably, bubbles in the snow ice layer scattered less energy than the depth hoar crystals over the adjacent ice surface resulting in warmer brightness temperatures over the fractures. Brightness temperatures of a continuous and deeper snowcover at the northwest end of the lake were low compared to the combined radiance of snowdrifts and pockets of bare ice across the lake surface.					
14. SUBJECT TERMS Freshwater ice Passive microwave imagery Snow				15. NUMBER OF PAGES 36	
				16. PRICE CODE	
17. SECURITY CLASSIFICATION OF REPORT UNCLASSIFIED	18. SECURITY CLASSIFICATION OF THIS PAGE UNCLASSIFIED	19. SECURITY CLASSIFICATION OF ABSTRACT UNCLASSIFIED	20. LIMITATION OF ABSTRACT UL		